Optics Letters

Ptychographic image reconstruction with a phase-assisted alternating direction method of multipliers

LI SONG,[1,*] KAIQIANG WANG,[2] SHUO ZHU,[3] ZHENBO REN,[2,4] AND EDMUND Y. LAM[3,5]

[1]School of Science, Northwest A&F University, Yangling 712100, China
[2]Key Laboratory of Light Field Manipulation and Information Acquisition, Ministry of Industry and Information Technology, and Shaanxi Key Laboratory of Optical Information Technology, School of Physical Science and Technology, Northwestern Polytechnical University, Xi'an 710129, China
[3]Department of Electrical and Electronic Engineering, The University of Hong Kong, Pokfulam, Hong Kong SAR, China
[4]zbren@nwpu.edu.cn
[5]elam@eee.hku.hk
*songli@nwafu.edu.cn

Received 20 December 2024; revised 28 February 2025; accepted 11 March 2025; posted 11 March 2025; published 17 April 2025

Ptychography is a widely used coherent imaging technique across many imaging modalities, especially microscopy. Reconstruction algorithms are important to obtain the final imaging results from a series of captured diffraction patterns. Conventional reconstruction algorithms only regard phase retrieval as an intermediate step in each iteration. The retrieved phase is lost and cannot be used in the following iterations. In this Letter, we introduce an auxiliary variable related to the phase information of the diffraction patterns in the iterative algorithms, which can make the history phase information available for future iterations. Simulation and experimental results show that our algorithm can achieve higher-quality reconstruction results than other commonly used algorithms.

https://doi.org/10.1364/OL.553571

Introduction. Coherent diffraction imaging (CDI) [1] is a typical phase imaging technique that can help to obtain the intensity and phase information of the target object. Coherent light transmits through the object, and imaging sensors are used to capture the far-field diffraction patterns. To extend the field of view (FOV) of the CDI system, ptychography [2] is introduced as a probe scanning imaging system. An object is scanned with partial overlap, and finally, a series of diffraction patterns are captured. This system is proven to be efficient in various applications, such as biological imaging [3] and material analysis [4].

Since the phase information of the diffraction pattern is lost during the capturing process, phase retrieval [5] is of great importance to the reconstruction algorithms. The general Fourier phase retrieval tries to find the solution $\boldsymbol{x}$ of the equation described below:

$$\boldsymbol{y} = |F\boldsymbol{x}|, \tag{1}$$

where $\boldsymbol{y}$ is the vectorized diffraction pattern, F is the 2D Fourier matrix with a compatible dimension, and $\boldsymbol{x}$ is the image of the target object. If the exact phase information $\boldsymbol{\phi}_t$ attached to $\boldsymbol{y}$ is known, then $\boldsymbol{x}$ can be obtained by the inverse Fourier transform of $\boldsymbol{y} \circ \boldsymbol{\phi}$ ($\circ$ is the Hadamard product), where we define phase vector $\boldsymbol{\phi} = \exp(i * \boldsymbol{\phi}_t)$ for simplicity.

Alternating algorithms are first used to solve this problem, such as the Gerchberg and Saxton method (GS) [6] and hybrid input–output algorithm (HIO) [7]. Another idea is to convert Eq. (1) to an optimization problem, and then it can be solved by different kinds of optimization methods [8]. These methods usually require more computation. Deep learning methods can also be used to solve this problem; they can automatically learn the mapping from the measurements to the objects [9]. These methods can also be combined with the physical model or other prior knowledge to improve the performances [10–12].

Alternating direction method of multipliers (ADMM) [13] is a combination of these two ideas. It is an optimization method that is designed based on the alternating strategy. This algorithm is suitable for solving the phase retrieval problem in different imaging systems including CDI [14,15] and ptychography [16].

Conventional reconstruction algorithms for ptychography [17], such as ptychographical iterative engine (PIE) [2], extended PIE (ePIE) [18], and regularized PIE (rPIE) [19], only consider the phase retrieval as an intermediate process, and the retrieved phase during the iterations is lost and cannot be used in the following iterations. As is shown in Fig. 1, the phase information of the diffraction pattern is only used in the modulus replacement step, and then it is lost again and can only be used in the next iteration indirectly. In this Letter, similar to the object and probe, we regard the phase vector $\boldsymbol{\phi}$ as part of the output variables in one iteration, and then its history information can be used in the following iteration, which can provide help to the reconstruction process.

Method. For a conventional ptychographic imaging model, raster scan is used to capture a series of diffraction patterns related to different parts of the target object. For each scan point,

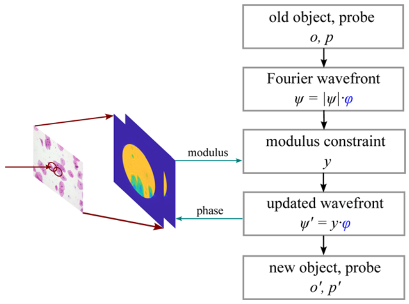

Fig. 1. Phase information in the conventional reconstruction algorithms. The phase information in the Fourier domain (blue part) is retrieved in each iteration, but it is lost again after this iteration since only the information in the object plane (o, p) is recorded.

if the detector is placed in the far field, then the imaging model is the same as the CDI setup. Mathematically, the imaging model for the j^{th} position can be described as follows [2]:

$$I_j(\boldsymbol{u}) = \left|\mathcal{F}\{P(\boldsymbol{r}) \circ O_j(\boldsymbol{r})\}\right|^2, \tag{2}$$

where $\boldsymbol{r}$ and $\boldsymbol{u}$ are the real-space and reciprocal-space coordinates, $O \in \mathbb{C}^{n_1\times n_2}$ is the object wavefront and $O_j \in \mathbb{C}^{m_1\times m_2}$ is the illuminating region in the current scan, $P \in \mathbb{C}^{m_1\times m_2}$ is the probe wavefront, and $I_j(\boldsymbol{u}) \in \mathbb{C}^{m_1\times m_2}$ is the captured diffraction pattern at the j^{th} scanning position $(j = 1, 2, \ldots, N)$. For simplicity, we omit the variables in the bracket, and the imaging model can be simplified as follows:

$$\sqrt{I_j} \circ \Phi_j = \mathcal{F}\{P \circ O_j\}, \tag{3}$$

where Φ_j is the missing phase related to the captured diffraction pattern. After vectorization, the imaging model can be described as follows:

$$\boldsymbol{y}_j \circ \boldsymbol{\phi}_j = F(\boldsymbol{m_p} \circ \boldsymbol{o}_j), \tag{4}$$

where $\boldsymbol{y}_j$, $\boldsymbol{\phi}_j$, $\boldsymbol{m_p}$, and $\boldsymbol{o}_j$ are the vectors from the vectorization of 2D matrices $\sqrt{I_j}$, Φ_j, P, and O_j, and F is the 2D Fourier matrix. However, for this expression, the relationships among different $\boldsymbol{o}_j$ are not identified clearly. With reference to the expression in [16], we can use a binary matrix S_j with a dimension $m_1m_2 \times n_1n_2$ to describe the j^{th} scanning region of the object, and then we can obtain the following:

$$\boldsymbol{y}_j \circ \boldsymbol{\phi}_j = F(\boldsymbol{m_p} \circ S_j\boldsymbol{o}). \tag{5}$$

In this setup, S_j is a downsampling matrix that is not a square. As a special case, if S_j is an identity matrix, then $j = 1$, and this imaging model is identical to the masked CDI setup.

For Eq. (5), letting $\boldsymbol{\psi}_j = \boldsymbol{m_p} \circ S_j\boldsymbol{o}$, a constrained optimization problem with regularization functions for the unknown variables can be obtained as follows:

$$\text{minimize} \quad \sum_{j=1}^{N} R(\boldsymbol{\phi}_j) + \sum_{j=1}^{N} \frac{1}{2}\|\boldsymbol{y}_j \circ \boldsymbol{\phi}_j - F\boldsymbol{\psi}_j\|_2^2 \tag{6}$$

$$\text{subject to} \quad \boldsymbol{\psi}_j - \boldsymbol{m_p} \circ S_j\boldsymbol{o} = 0, \quad j = 1, 2, \ldots, N. \tag{7}$$

where $R(\boldsymbol{\phi})$ is an indicator function defined as follows:

$$R(\boldsymbol{\phi}) = \begin{cases} 0, & |\boldsymbol{\phi}| = \mathbf{1} \\ \infty, & \text{otherwise} \end{cases}. \tag{8}$$

Accordingly, the Lagrangian can be expressed as follows:

$$\begin{aligned} L(\boldsymbol{\phi}_j, \boldsymbol{\psi}_j, \boldsymbol{m_p}, \boldsymbol{o}, \boldsymbol{\mu}_j) = {} & \sum_{j=1}^{N} R(\boldsymbol{\phi}_j) + \sum_{j=1}^{N} \frac{1}{2}\|\boldsymbol{y}_j \circ \boldsymbol{\phi}_j - F\boldsymbol{\psi}_j\|_2^2 \\ & + \sum_{j=1}^{N} \frac{\rho_j}{2}\|\boldsymbol{\psi}_j - \boldsymbol{m_p} \circ S_j\boldsymbol{o} + \boldsymbol{\mu}_j\|_2^2, \end{aligned} \tag{9}$$

and then we can write the iterative form as follows (derivations can be found in Supplement 1):

$$\boldsymbol{\psi}_j{}^{k+1} = (F^HF + \rho_jI)^{-1}[F^H(\boldsymbol{y_j} \circ \boldsymbol{\phi}_j{}^k) + \rho_j(\boldsymbol{m_p}{}^k \circ S_j\boldsymbol{o}^k - \boldsymbol{\mu}_j{}^k)], \tag{10}$$

$$\boldsymbol{\phi}_j{}^{k+1} = \text{proj}_R(F\boldsymbol{\psi}_j{}^{k+1}), \tag{11}$$

$$\boldsymbol{o}^{k+1} = \arg\min_{\boldsymbol{o}} \frac{1}{2}\|\boldsymbol{\psi}_j{}^{k+1} - \boldsymbol{m_p}{}^k \circ S_j\boldsymbol{o} + \boldsymbol{\mu}_j{}^k\|_2^2, \tag{12}$$

$$\boldsymbol{m_p}{}^{k+1} = \arg\min_{\boldsymbol{m_p}} \frac{1}{2}\|\boldsymbol{\psi}_j{}^{k+1} - \boldsymbol{m_p} \circ S_j\boldsymbol{o}^{k+1} + \boldsymbol{\mu}_j{}^k\|_2^2, \text{ and} \tag{13}$$

$$\boldsymbol{\mu}_j{}^{k+1} = \boldsymbol{\mu}_j{}^k + \boldsymbol{\psi}_j{}^{k+1} - \boldsymbol{m_p}{}^{k+1} \circ S_j\boldsymbol{o}^{k+1}, \tag{14}$$

where proj_R is a projection operator with respect to the feasible domain of the indicator function R. According to the property of the Fourier matrix, $F^HF = m_1m_2I$. The effect of introducing a new variable $\boldsymbol{\phi}$ is shown in Eq. (10). The value of $\boldsymbol{\psi}$ is expected to be the wavefront in the object plane. In conventional algorithms, it is only determined by $\boldsymbol{o}$ and $\boldsymbol{m_p}$, such as for a general ADMM method, the $\boldsymbol{\psi}$-update step can be expressed as follows:

$$\boldsymbol{\psi}_j{}^{k+1} = F^{-1}\{\boldsymbol{y}_j \circ \text{proj}_R[F(\boldsymbol{m_p}{}^k \circ S_j\boldsymbol{o}^k - \boldsymbol{\mu}_j{}^k)]\}. \tag{15}$$

However, in Eq. (10), current estimation in the Fourier plane $\boldsymbol{y_j} \circ \boldsymbol{\phi}_j{}^k$ is also considered.

For the update steps with the object and probe, if we solve the update steps related to $\boldsymbol{o}$ and $\boldsymbol{m_p}$ directly, the minimization problems are unstable [20]. Adding a proximal regularizer can help to solve this problem without changing the convergence results. Now, these two update steps can be obtained by solving the optimization problem:

$$\boldsymbol{o}^{k+1} = \arg\min_{\boldsymbol{o}} \frac{1}{2}\|\boldsymbol{m_p}{}^k \circ S_j\boldsymbol{o} - \boldsymbol{\psi}_j{}^{k+1} - \boldsymbol{\mu}_j{}^k\|_2^2 + \frac{1}{2t_1}\|\boldsymbol{o} - \boldsymbol{o}^k\|_2^2, \tag{16}$$

$$\boldsymbol{m_p}{}^{k+1} = \arg\min_{\boldsymbol{m_p}} \frac{1}{2}\|\boldsymbol{m_p} \circ S_j\boldsymbol{o}^{k+1} - \boldsymbol{\psi}_j{}^{k+1} - \boldsymbol{\mu}_j{}^k\|_2^2 + \frac{1}{2t_2}\|\boldsymbol{m_p} - \boldsymbol{m_p}{}^k\|_2^2. \tag{17}$$

Taking the gradient of Eq. (16) and setting it to 0, we will obtain the closed-form solution. To deal with the Hardmard product, we introduce a diagonal matrix M_p with $\text{diag}(M_p) = \boldsymbol{m_p}$. Now, $\boldsymbol{m_p}{}^k \circ S_j\boldsymbol{o}$ can be expressed as $M_pS_j\boldsymbol{o}$, and the $\boldsymbol{o}$-update step can be expressed as follows:

$$\boldsymbol{o}^{k+1} = (t_1S_j^HM_p^{(k)H}M_p^{(k)}S_j + I)^{-1}[t_1S_j^HM_p^{(k)H}(\boldsymbol{\psi}_j{}^{k+1} + \boldsymbol{\mu}_j{}^k) + \boldsymbol{o}^k]. \tag{18}$$

Since S_j is a sampling matrix and M_p is a diagonal matrix, the inverse matrix is also a diagonal matrix.

With the same idea, we set $\text{diag}(O_j) = S_j\boldsymbol{o}$ and now $\boldsymbol{m_p} \circ S_j\boldsymbol{o}^{k+1} = O_j^{k+1}\boldsymbol{m_p}$. The $\boldsymbol{m_p}$-update step can be obtained as follows:

$$\boldsymbol{m_p}{}^{k+1} = (t_2O_j^{(k+1)H}O_j^{(k+1)} + I)^{-1}[t_2O_j^{(k+1)H}(\boldsymbol{\psi}_j{}^{k+1} + \boldsymbol{\mu}_j{}^k) + \boldsymbol{m_p}{}^k]. \tag{19}$$

Finally, we summarize these steps, and the ADMM iterations for the ptychographic phase retrieval problem are given in Algorithm 1.

Algorithm 1. Phase-assisted ADMM (P-ADMM) for ptychography

Input: $\boldsymbol{y}_j$: captured diffraction patterns; $\boldsymbol{\phi}_j{}^0, \boldsymbol{o}^0, \boldsymbol{m_p}{}^0, \boldsymbol{\mu}_j{}^0$: initial values; ρ_j, t_1, t_2: penalty parameters; n_{iter}: maximum number of iterations; ϵ_{tol}: error tolerance. $(j = 1, 2, \cdots, N)$.
Output: $\boldsymbol{o}$: reconstructed complex-valued image.

for $k = 1 : n_{\text{iter}}$ **do**
  for $j \in \{1, 2, \cdots, N\}$ **do**
    $\boldsymbol{\psi}_j{}^{k+1} = (F^H F + \rho_j I)^{-1}[F^H(\boldsymbol{y_j} \circ \boldsymbol{\phi}_j{}^k) + \rho_j(\boldsymbol{m_p}{}^k \circ S_j \boldsymbol{o}^k - \boldsymbol{\mu}_j{}^k)]$,
    $\boldsymbol{\phi}_j{}^{k+1} = \text{proj}_R(F\boldsymbol{\psi}_j{}^{k+1})$,
    $\boldsymbol{o}^{k+1} = (t_1 S_j^H M_p^{(k)H} M_p^{(k)} S_j + I)^{-1}[t_1 S_j^H M_p^{(k)H}(\boldsymbol{\psi}_j{}^{k+1} + \boldsymbol{\mu}_j{}^k) + \boldsymbol{o}^k]$,
    $\boldsymbol{m_p}{}^{k+1} = (t_2 O_j^{(k+1)H} O_j^{(k+1)} + I)^{-1}[t_2 O_j^{(k+1)H}(\boldsymbol{\psi}_j{}^{k+1} + \boldsymbol{\mu}_j{}^k) + \boldsymbol{m_p}{}^k]$,
    $\boldsymbol{\mu}_j{}^{k+1} = \boldsymbol{\mu}_j{}^k + \boldsymbol{\psi}_j{}^{k+1} - \boldsymbol{m_p}{}^{k+1} \circ S_j \boldsymbol{o}^{k+1}$,
    $\epsilon_j = \left\| |F(\boldsymbol{m_p}{}^{k+1} \circ S_j \boldsymbol{o}^{k+1})| - \boldsymbol{y}_j \right\|_2^2$,
  $\epsilon(k) = \sum_{j=1}^N \epsilon_j \Big/ \sum_{j=1}^N \left\| \boldsymbol{y}_j \right\|_2^2$,
  if $\epsilon(k) < \epsilon_{\text{tol}}$ **then**
    break;
return $\boldsymbol{o}$

Note that j is chosen from a random order of 1 to N. The error term is calculated to be the ℓ_2-norm of the difference between the estimated and the captured diffraction patterns.

Results. To validate the efficiency of our method, we try our algorithm on the simulation experiment for electron ptychography. For the ground truth image, we simulate a complex object related to corn stunt spiroplasma [21]. For the ptychographic imaging model, the scan dimension is 20×20 with a step size of 3 nm for both directions, no rotation is added, and the sensor has a 128×128 resolution with a pixel size of 5.12 Å. The aperture size is 10 mrad, and the beam voltage is 300 keV. After the diffraction patterns are generated, 20% Gaussian noise is added, leading to the SNR of nearly 13.76 dB, which is a high noise level in real experiments. Finally, the simulated dataset is a matrix with a $128 \times 128 \times 400$ size, which is related to the value of $\boldsymbol{y}$ in the algorithm. More descriptions of these parameters are given in Supplement 1.

For the algorithm parameter setup in P-ADMM, the maximum number of iterations is set to be 100, and the initial probe can be calculated according to the experimental setup. The initial phase $\boldsymbol{\phi}_j{}^0$ and object $\boldsymbol{o}^0$ are set to be the one vectors, and other initial vectors are zero vectors. The error tolerance is 9.2% based on the trial and error strategy, leading to the result of 62 iterations. For the penalty parameters, ρ_j is set to be $0.1 \times m_1 m_2$ in order to make it compatible with the value of $F^H F$ in Eq. (10). With reference to the design of the ePIE algorithm, t_1 and t_2 in this algorithm are chosen to be as follows [20]:

$$t_1 = \frac{\beta_0}{(1 - \beta_0)|M_p^{(k)}|^2_{\max}}, \tag{20}$$

$$t_2 = \frac{\beta_1}{(1 - \beta_1)|O_j^{(k+1)}|^2_{\max}}. \tag{21}$$

In our algorithm, the two parameters are $\beta_0 = \beta_1 = 0.01$, and then we can calculate t_1 and t_2 during the iterations. Sensitivity analysis is given in Supplement 1. We compare the results from our method with another two methods based on the conventional ADMM and ePIE. The parameter setup for ADMM is identical with the P-ADMM method. For ePIE, the two parameters are also set as 0.01, and we run 100 iterations for the ePIE algorithm.

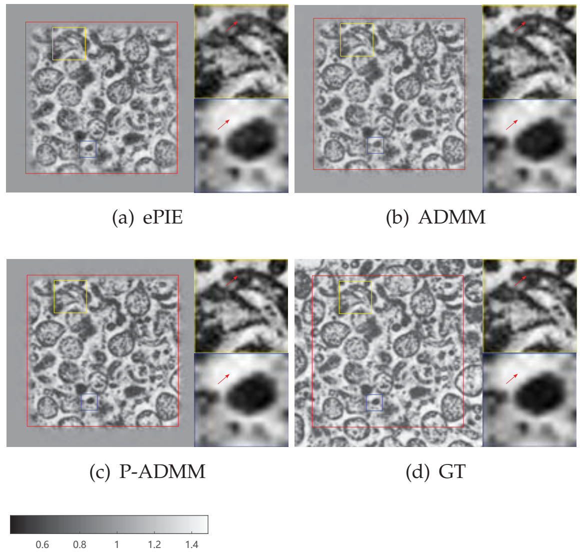

Fig. 2. Reconstruction results with different algorithms. Yellow and blue boxes show zoom-in views from different regions, while red box shows the region where SSIM is calculated below.

Table 1. Quantitative Evaluation Results[a]

	ePIE	ADMM	P-ADMM
SSIM	0.862	0.916	**0.947**
SSIM (full)	0.330	0.353	**0.365**

[a]The SSIM value shows the similarity of the region inside the red box in Fig. 2, while the full SSIM evaluates the whole image.

Reconstruction results from different algorithms are shown in Fig. 2. We can find that the P-ADMM result has a bit larger FOV than ADMM, while the reconstruction result from ePIE has the smallest FOV among these algorithms. Larger FOV means more useful information can be reconstructed from the same dataset. As is shown in the figure, more textures of the cells on the boundary from the P-ADMM result can be recognized. For the zoom-in result, P-ADMM achieves the least artifacts, while the cell images from other results are blurred with more noisy pixels. Overall, P-ADMM achieves the best performance among them.

Quantitative results are given in Table 1, where we calculate the structural similarity index matrix (SSIM) for the red region and full image, respectively. The red region is the region of interest (ROI) that contains most of the valid information from the reconstruction algorithms; hence, the evaluation within this region can show the reconstruction quality in ROI. We also evaluate the quality of the full image that can show the FOV of different reconstructions quantitatively. Among the three algorithms, P-ADMM has the highest SSIM, which complies with the visual results. To show the robustness of our method, more results with Poisson noise and scan position errors are given in Supplement 1.

All these algorithms are in an iterative style; now, we analyze the differences among these algorithms. The ePIE method is just an alternating method between the object plane and sensor plane, and gradient descent is used for updates of the object and

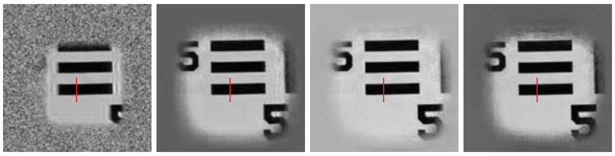

(a) ePIE (b) rPIE (c) sDR (d) P-ADMM

Fig. 3. Experimental reconstruction results for the USAF resolution target with different algorithms.

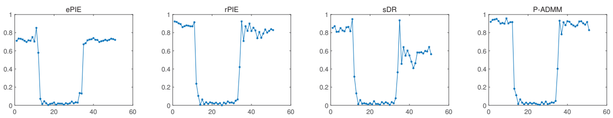

(a) ePIE (b) rPIE (c) sDR (d) P-ADMM

Fig. 4. Zoom-in results in the red line regions for the USAF resolution target from different algorithms.

probe in order to minimize the residual. The main difference between the ADMM method and ePIE is that dual variable $\boldsymbol{\mu}$ is introduced, which is an integral of the residual as is shown in Eq. (14). With this step, the history information of the residual can be used, making it easier to achieve an optimal point. P-ADMM has the same idea, but it further takes advantages of the phase information, and then the old and new estimations of the wavefront from the Fourier plane can be used in Eq. (10). The history information of the residual and phase makes our algorithm achieve higher reconstruction quality.

We also test our algorithm on a real experimental ptychographic dataset collected by [20]. More descriptions of the experimental setup are given in Supplement 1. We follow the official numerical setup, and the sparsity test is given by choosing half of all the diffraction patterns. The penalty parameters in P-ADMM are set as $\beta_0 = 0.9, \beta_1 = 0.5, \rho_j = 0.7/(1-0.7) \times m_1 m_2$, based on the parameter setups of ePIE. The initial aperture is set to be a pinhole with a radius of 75 µm. The initial object has a random phase with the amplitude set to be 1. Other initial variables are identical with the setup in the simulation experiment.

For this experiment, we compare our results with the ePIE [18], rPIE [19], and sDR [20] methods, and we run 100 iterations for all the algorithms. Since for P-ADMM, warm start with 30 iterations is used, 70 iterations remain for our algorithm. Visual results with the amplitude information are summarized in Fig. 3. For a more intuitive comparison, we show the zoom-in results for the red line regions in Fig. 4. We can find that ePIE has the smallest FOV, rPIE and sDR have larger FOV but more background noise in the center region, and P-ADMM has both larger FOV and less noise (smoother lines in Fig. 4), leading to the best reconstruction quality for this setup.

For quantitative evaluations, we calculate the R-factor that evaluates the relative residual in the measurement domain, and the results are given in Table 2. Convergence curves can be found in Supplement 1. We can find that P-ADMM has the lowest R-factor, which shows that our reconstruction has the least error in the measurement domain. Since in P-ADMM, a new variable $\boldsymbol{\phi}$ related to the phase information is added as the main variable, its convergence property is also considered during the iterations and presented in the final convergence curve; hence, it has better convergence behavior than ADMM.

Table 2. R-Factor of the Reconstruction Results from Different Algorithms[a]

	ePIE	rPIE	sDR	P-ADMM
R-factor	16.13%	13.10%	12.41%	**11.53%**

[a]Lower is better.

In conclusion, we propose a new reconstruction algorithm for ptychography based on the retrieving process of the phase information in the measurement domain. The retrieved phase can help with the following iterations. Besides, the Lagrangian variable in the ADMM is related to the integration of the residual in the object domain. Both of these two parts take advantages of the history information during the iterations, which can help to improve the quality of the reconstruction results.

Funding. Scientific Startup Foundation for Doctors of Northwest A and F University (Z1090124023); Research Grants Council of Hong Kong (GRF 17201822, RIF 7003-21, GRF 17200321).

Disclosures. The authors declare no conflicts of interest.

Data availability. Experimental data underlying the USAF results can be found in [20].

Supplemental document. See Supplement 1 for supporting content.

REFERENCES

1. J. Miao, P. Charalambous, J. Kirz, *et al.*, Nature **400**, 342 (1999).
2. J. M. Rodenburg and H. M. Faulkner, Appl. Phys. Lett. **85**, 4795 (2004).
3. T. Wang, P. Song, S. Jiang, *et al.*, Opt. Lett. **48**, 485 (2023).
4. S. Gao, P. Wang, F. Zhang, *et al.*, Nat. Commun. **8**, 163 (2017).
5. Y. Shechtman, Y. C. Eldar, O. Cohen, *et al.*, IEEE Signal Process. Mag. **32**, 87 (2015).
6. R. W. Gerchberg and W. O. Saxton, Optik **35**, 237 (1972).
7. J. R. Fienup, Appl. Opt. **21**, 2758 (1982).
8. E. J. Candès, X. Li, and M. Soltanolkotabi, IEEE Trans. Inf. Theory **61**, 1985 (2015).
9. K. Wang, L. Song, C. Wang, *et al.*, Light: Sci. Appl. **13**, 4 (2024).
10. L. Song and E. Y. Lam, Opt. Express **31**, 10386 (2023).
11. Z. Wang, S. Zheng, Z. Ding, *et al.*, J. Opt. Soc. Am. A **41**, 165 (2024).
12. Y. Yang, Z. Li, X. Yang, *et al.*, Opt. Lett. **49**, 6701 (2024).
13. S. Boyd, N. Parikh, E. Chu, *et al.*, *Distributed Optimization and Statistical Learning via the Alternating Direction Method of Multipliers* (Now Publishers Inc., 2011).
14. L. Song and E. Y. Lam, Photonics Res. **10**, 758 (2022).
15. L. Song and E. Y. Lam, Opt. Express **30**, 25788 (2022).
16. H. Chang, P. Enfedaque, and S. Marchesini, SIAM J. Imaging Sci. **12**, 153 (2019).
17. S. Jiang, P. Song, T. Wang, *et al.*, Nat. Protoc. **18**, 2051 (2023).
18. A. M. Maiden and J. M. Rodenburg, Ultramicroscopy **109**, 1256 (2009).
19. A. Maiden, D. Johnson, and P. Li, Optica **4**, 736 (2017).
20. M. Pham, A. Rana, J. Miao, *et al.*, Opt. Express **27**, 31246 (2019).
21. Cell Image Library, "Electron micrograph of corn stunt spiroplasma," https://www.cellimagelibrary.org/images/12578.